ACS APPLIED MATERIALS & INTERFACES

www.acsami.org

Research Article

High Quality Factors in Superlattice Ferroelectric $Hf_{0.5}Zr_{0.5}O_2$ Nanoelectromechanical Resonators

Xu-Qian Zheng, Troy Tharpe, S M Enamul Hoque Yousuf, Nicholas G. Rudawski, Philip X.-L. Feng, and Roozbeh Tabrizian*

Cite This: *ACS Appl. Mater. Interfaces* 2022, 14, 36807−36814

Read Online

ACCESS | Metrics & More | Article Recommendations | Supporting Information

ABSTRACT: The discovery of ferroelectricity and advances in creating polar structures in atomic-layered hafnia-zirconia ($Hf_xZr_{1-x}O_2$) films spur the exploration of using the material for novel integrated nanoelectromechanical systems (NEMS). Despite its popularity, the approach to achieving high quality factors (Qs) in resonant NEMS made of $Hf_xZr_{1-x}O_2$ thin films remains unexplored. In this work, we investigate the realization of high Qs in $Hf_{0.5}Zr_{0.5}O_2$ nanoelectromechanical resonators by stress engineering via the incorporation of alumina (Al_2O_3) interlayers. We fabricate nanoelectromechanical resonators out of the $Hf_{0.5}Zr_{0.5}O_2$-Al_2O_3 superlattices, from which we measure Qs up to 171,000 and frequency−quality factor products ($f \times Q$) of $>10^{11}$ Hz through electrical excitation and optical detection schemes at room temperature in vacuum. The analysis suggests that clamping loss and surface loss are the limiting dissipation sources and $f \times Q > 10^{12}$ Hz is achievable through further engineering of anchor structure and built-in stress.

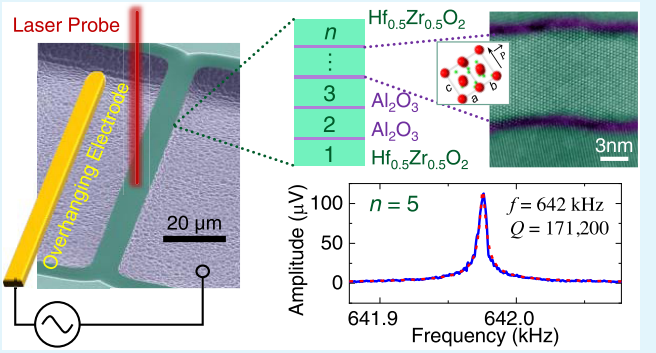

KEYWORDS: *hafnia-zirconia ($Hf_xZr_{1-x}O_2$), ferroelectric, resonator, energy dissipation, stress engineering*

INTRODUCTION

Hafnia-zirconia ($Hf_xZr_{1-x}O_2$) has recently emerged as a material to enable nanoscale ferroelectric films with promising potential for the realization of the "more-than-Moore" paradigm within CMOS platforms.[1−3] Hafnia-zirconia films, deposited by atomic layer deposition (ALD) and in amorphous form, have been widely adopted as a high-κ dielectric in high-performance transistors. The observation of ferroelectricity in hafnia-zirconia, over a limited thickness range and once subjected to proper thermomechanical treatments, provides the unprecedented opportunity of having a multifunctional material in advanced semiconductor nodes. Over the past decade, nanoscale ferroelectric hafnia-zirconia films have been developed and explored for diverse applications, including ultralow-power memory and computing,[3−7] energy harvesting and storage,[8,9] and sensing and actuation.[10−12]

In addition to the superior processing and integration benefits, the transforming advantage of hafnia-zirconia over conventional perovskite or emerging nitride ferroelectrics is its ability to sustain robust polarization when scaled to sub-10 nm thicknesses.[2,13,14] This unique dimensional scalability is not only pivotal for the realization of dense memory devices on advanced CMOS nodes but also highly favorable for the creation of high-performance nanoelectromechanical systems (NEMS).[11,12,15]

Ultrascaled hafnia-zirconia piezoelectric transducers, with thicknesses of just a few nanometers, favor the creation of integrated NEMS sensors with enhanced detection limits.[16−18] Furthermore, the extreme thickness scalability, while sustaining piezoelectricity, augurs the promising potential of hafnia-zirconia to create integrated high-quality-factor (Q) NEMS resonators. Thickness-mode bulk acoustic wave resonance can be excited using the sustained longitudinal piezoelectric coefficient of hafnia-zirconia, even at the nanometer scale.[19,20] Therefore, sub-50 nm hafnia-zirconia transducers enable the realization of NEMS resonators with frequencies extending to centimeter and millimeter wave regimes. This is highly desirable for the realization of modern wireless communication systems that target the use of wide cm and mm wave spectrum to fulfill the massive data rate and ultralow-latency requirements of emerging applications such as metaverse, connected vehicles, internet of things, etc.[11,12,21]

Realization of high-performance hafnia-zirconia NEMS resonators requires quantitative understanding of the govern-

Received: May 12, 2022
Accepted: July 22, 2022
Published: August 3, 2022

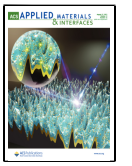

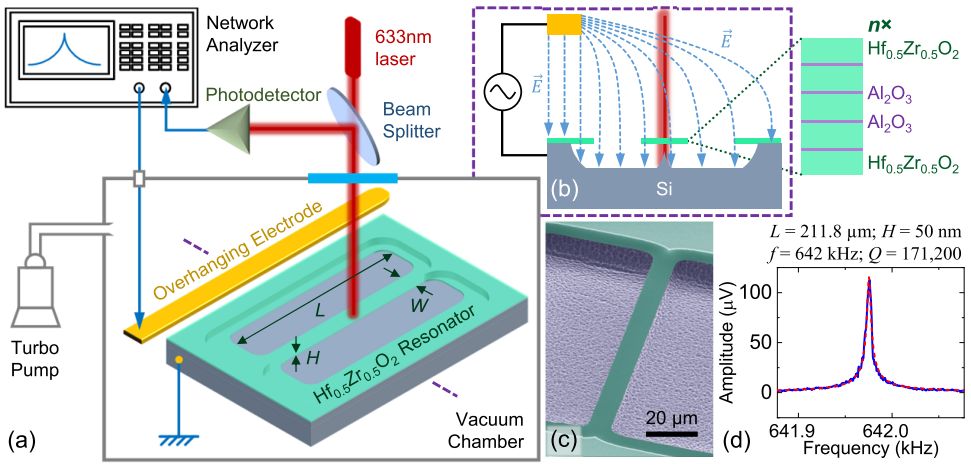

Figure 1. Resolving the resonance characteristics of nanolaminated $Hf_{0.5}Zr_{0.5}O_2$ nanoelectromechanical resonators through noncontact electrical driving and optical detection. (a) Schematic of the measurement apparatus with an overhanging electrode for electrical driving of device motion and a 633 nm laser for the interferometric detection of device motion. The length, width, and thickness of the device are labeled as *L*, *W*, and *H*, respectively. (b) Cross-sectional view of the measurement scheme along with the cross section of the layer stacking. (c) Colored scanning electron microscopy (SEM) image of a doubly clamped $Hf_{0.5}Zr_{0.5}O_2$ nanoresonator. (d) A typical measured resonance spectrum of a $Hf_{0.5}Zr_{0.5}O_2$ nanoresonator.

ing energy dissipation mechanisms limiting *Q*. Such understanding is not trivial, considering the complex crystal structures of hafnia-zirconia with the coexistence of multiple phases and strong dependence of morphology and energy dynamics on mechanical boundary conditions. Further, the nanoscale thickness of the film and the resulting large surface-to-volume ratio may induce excess energy dissipation and impose limitations on the nondestructive exploration of dissipation dynamics. This is mainly due to the small mechanical energy that can be stored in ultrathin hafnia-zirconia NEMS, with respect to geometrical and energy localization imperfections, and its corresponding effects on *Q*. The understanding of intrinsic electromechanical energy dissipation limits also sheds light on the ultimate power consumption limit in emerging nanoscale and ultralow-power ferroelectric hafnia memory devices for neuromorphic computing.[3,5−7]

In this work, we explore stress engineering to significantly enhance the energy density in hafnia-zirconia NEMS by using alumina (Al_2O_3) interlayers to create $Hf_{0.5}Zr_{0.5}O_2$-Al_2O_3 superlattices. This enables the achievement of high *Q* in $Hf_{0.5}Zr_{0.5}O_2$ NEMS resonators, through stress-enhanced dilution of energy dissipation. We develop $Hf_{0.5}Zr_{0.5}O_2$ NEMS resonators along with a noncontact electrical excitation and optical motion detection scheme for accurate quantification of energy dissipation and *Q* with respect to variations in transducer thickness and superlattice configuration. We also analyze the dissipation pathways in $Hf_{0.5}Zr_{0.5}O_2$ nanoelectromechanical resonators and give guidelines for further enhancing the *Q* in such resonators.

METHODS AND MATERIALS

Ferroelectric $Hf_{0.5}Zr_{0.5}O_2$ nanoresonators take the form of a clamped-clamped structure as shown in Figure 1. The functional layer is a nanolamination that consists of ∼9 nm thick $Hf_{0.5}Zr_{0.5}O_2$ layers intercalated by 1 nm thick Al_2O_3 layers to maintain the ferroelectric (orthorhombic) phase of $Hf_{0.5}Zr_{0.5}O_2$ (Figure 1b). The stack is synthesized in a single ALD run, followed by rapid thermal annealing (RTA) at 500 °C in nitrogen for 20 s. Detailed fabrication process steps can be found in ref 15. Figure 1c shows a colored scanning electron microscopy (SEM) image of a typical ferroelectric $Hf_{0.5}Zr_{0.5}O_2$ nanoresonator in this work. The use of metal electrodes atop nanoresonators not only loads the resonator but also generates heat while driving device motion, degrading device performance. Therefore, to extract intrinsic device *Q* without these effects, we measure the resonance characteristics of devices through the combination of electromechanical motion excitation and optical interferometry detection. As shown in Figure 1a,b, an alternating electrical field is introduced by an electrode hanging hundreds of μm above the device, thus creating an alternating force to drive the device motion utilizing the piezoelectric effect in the $Hf_{0.5}Zr_{0.5}O_2$ material, without requiring electrodes patterned on the mechanical devices. The driven device motion is detected interferometrically by a 633 nm laser. The overhanging electrode is slightly aside from the device to not block the detection laser. A vacuum chamber connected to a turbo pump is used for achieving high vacuum of <5 mTorr. The measurement system provides combined benefits of (i) uniform driving force over the complete device without necessitating the otherwise loading and lossy electrodes on the devices, (ii) laser interferometry for ultrasensitive motion detection, and (iii) high vacuum environment for the removal of air damping effects. Figure 1d shows a typical fundamental mode resonance spectrum of a $Hf_{0.5}Zr_{0.5}O_2$ resonator in this work. Table S1 in the Supporting Information summarizes the measured resonance characteristics of all devices in this work, tested under pressures of <5 mTorr. The devices exhibit f−Q products on the order of 10^{11} Hz.

To characterize the ferroelectricity of atomic-layered $Hf_{0.5}Zr_{0.5}O_2$ nanolaminates, 120 × 120 μm^2 solidly mounted (i.e., unreleased) capacitors are also created in the same batch by sandwiching the dielectric stack between 20 nm thick tungsten (W) electrodes to enable electrical measurements. Figure 2a,b depicts the polarization−electric field and current−electric field hysteresis loops, respectively, measured for W/$Hf_{0.5}Zr_{0.5}O_2$/W capacitors with $Hf_{0.5}Zr_{0.5}O_2$ lamination varying from 10 nm (single layer) to 50 nm (five layers). Measured capacitors are subjected to the same ALD and RTA processes as $Hf_{0.5}Zr_{0.5}O_2$ nanoresonators, with measurements taken following application of 1000 bipolar, square, wake-up pulses at 1 kHz frequency. A stable remanent polarization (P_r) and gaussian switching current are measured for all cycled nanolaminates, confirming ferroelectricity in unreleased samples and therefore polar morphology in $Hf_{0.5}Zr_{0.5}O_2$ constituent layers. Electrical measurements of pristine (uncycled) capacitors are depicted in Figure S1 in the Supporting Information. Confirmation of film ferroelectricity within released, electrodeless, $Hf_{0.5}Zr_{0.5}O_2$ nanolaminates is achieved via grazing incident X-ray diffraction (GIXRD) analysis of ∼20 × 30 mm^2

https://doi.org/10.1021/acsami.2c08414
ACS Appl. Mater. Interfaces 2022, 14, 36807−36814

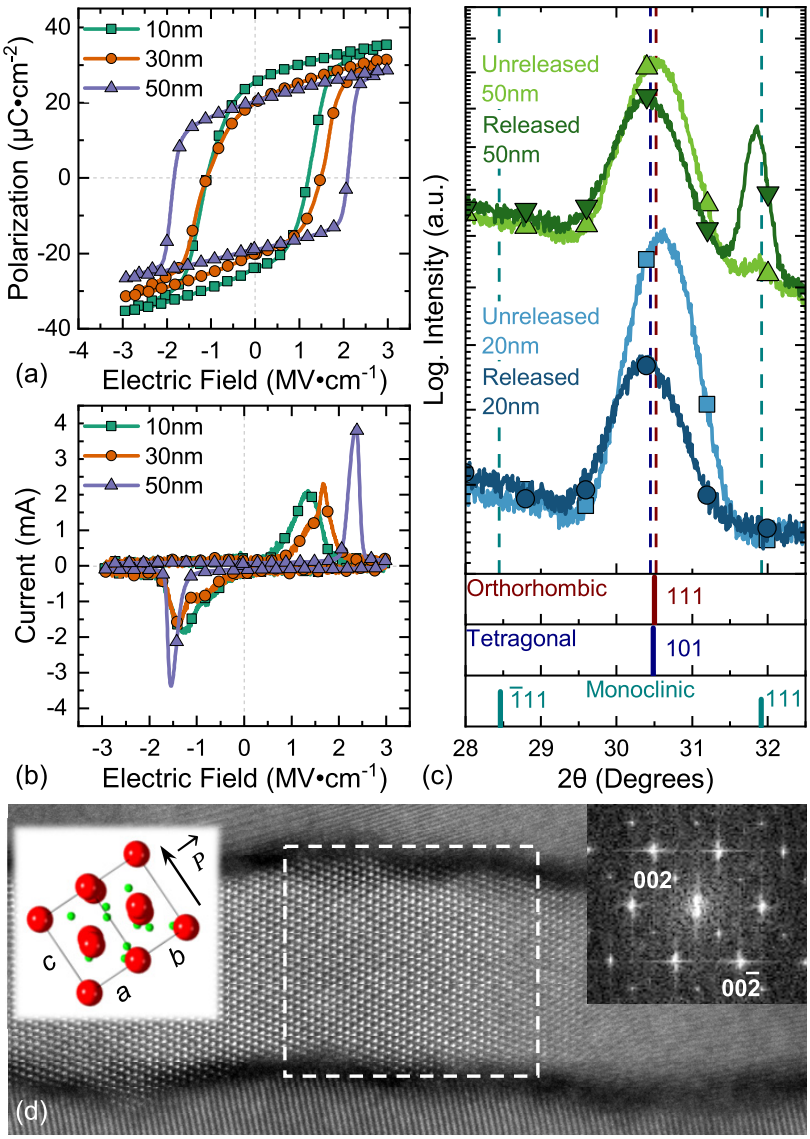

Figure 2. Ferroelectric characterization of nanolaminated $Hf_{0.5}Zr_{0.5}O_2$. (a) Polarization−electric field hysteresis loops for 10 nm (single $Hf_{0.5}Zr_{0.5}O_2$ layer), 30 nm (three $Hf_{0.5}Zr_{0.5}O_2$ layers), and 50 nm (five $Hf_{0.5}Zr_{0.5}O_2$ layers) capacitors with 20 nm W top and bottom electrodes after wake-up cycling. (b) Current−electric field hysteresis loops for capacitors identical to (a). (c) GIXRD scans of released and unreleased 20 nm (two $Hf_{0.5}Zr_{0.5}O_2$ layers) and 50 nm, electrodeless films fabricated according to process steps within Figure S2. (d) HAADF-STEM images of the $Hf_{0.5}Zr_{0.5}O_2$ layer within the nanolaminate stack from a pristine (uncycled) capacitor taken near the [110] zone axis. The right inset is a 2D FFT obtained from the selected area indicating a *c*-axis rotation of 34° counterclockwise, as shown in the left inset.

samples, shown in Figure 2c. Electrodeless membranes continue to exhibit a Bragg reflection peak at $2\theta = 30.5°$ even after the removal of electrodes and release by selective dry etching of W layers and Si substrate. This peak corresponds to the superimposed polar orthorhombic(111) and tetragonal(101) phases,[19,20,22] confirming the existence of a dominant polar morphology within released, electrodeless, $Hf_{0.5}Zr_{0.5}O_2$ nanolaminates. Interestingly, the release of 50 nm membranes results in the promotion of a nonpolar monoclinic(111) peak at $2\theta = 31.69°$. This can be attributed to a nonsymmetric stress gradient across thicker nanolaminates. Figure S2 in the Supporting Information depicts the fabrication process used to realize samples for GIXRD characterization, while Figures S3 and S4 show the optical images of released and unreleased 20 and 50 nm $Hf_{0.5}Zr_{0.5}O_2$ nanolaminates, respectively. To further resolve $Hf_{0.5}Zr_{0.5}O_2$ ferroelectricity, high-angle annular dark field scanning transmission electron microscopy (HAADF-STEM) images are taken for individual $Hf_{0.5}Zr_{0.5}O_2$ layers. Depicted in Figure 2d is a representative orthorhombic grain taken from a layer within the 50 nm $Hf_{0.5}Zr_{0.5}O_2$ nanolaminate. A two-dimensional fast Fourier transform (2D FFT) of the highlighted area reveals the grain to be orthorhombic with a polar (*c*-axis) tilt of 34°, counterclockwise from the surface normal.

RESULTS AND DISCUSSION

In general, it is desirable to achieve high *Q*s in M/NEMS resonators. The measured *Q* of a resonator is determined by the combined contributions of different dissipation processes in the resonator. Since $1/Q$ represents the energy dissipation, assuming uncorrelated energy loss mechanisms, the relation can be expressed using the equation

$$\left(\frac{1}{Q}\right)_{\text{Total}} = \left(\frac{1}{Q}\right)_{\text{TED}} + \left(\frac{1}{Q}\right)_{\text{Clamping}} + \left(\frac{1}{Q}\right)_{\text{Surface}} + \left(\frac{1}{Q}\right)_{\text{Air}} + \left(\frac{1}{Q}\right)_{\text{Other}} \quad (1)$$

https://doi.org/10.1021/acsami.2c08414
ACS Appl. Mater. Interfaces 2022, 14, 36807−36814

where $(1/Q)_{Total}$ is the total energy dissipation in the resonator and the rest are energy dissipation terms limited by thermoelastic damping (TED), clamping loss, surface loss, air damping, and other loss mechanisms. The equation indicates that a dissipation process with the smallest Q dominates the determination of the measured Q of the resonator. Other loss mechanisms consist of mechanisms that can be neglected in the $Hf_{0.5}Zr_{0.5}O_2$ resonators in this work, including dielectric loss and phonon−electron interaction, since there is no current going through the device, and phonon−phonon interaction with the Akhieser regime possessing the f−Q product of $>10^{13}$ Hz, much higher than the measured f−Q in this work.[23] Thus, we mainly investigate the first four terms on the right-hand side of eq 1.

Air damping is the only dissipation process limited by the environment among the four terms, so we can eliminate the air damping effect by controlling the environment, i.e., operating the device in a sufficiently high vacuum. Figure 3 shows the frequency f and Q of the fundamental mode under varying pressure for the longest (L = 211.8 μm) $Hf_{0.5}Zr_{0.5}O_2$ resonators with varied thicknesses in this work. Q saturates when pressure p < 5 mTorr, indicating the elimination of air damping as the major limiting factor of the total Q of the resonator. We measure all devices with p < 5 mTorr for device-intrinsic Q analysis by evading the air damping effects. In addition, Figure 3 shows that in higher pressure ranges, Q follows two different trends: $Q \propto p^{-1}$ and $Q \propto p^{-1/2}$. In the former trend, Q is limited by free molecule flow (FMF) damping, which is related to the energy dissipation process of the resonator striking free gas molecules in the environment and losing energy to them. For the latter, Q is limited by viscous damping.[24]

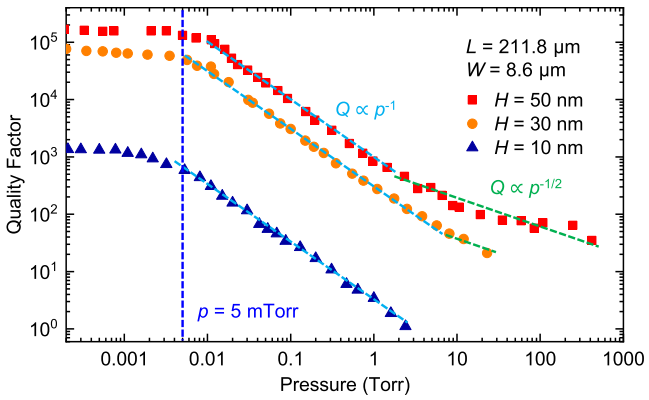

Figure 3. Mitigating the air damping effects on $Hf_{0.5}Zr_{0.5}O_2$ resonators. Q vs p in the range from 0.2 mTorr to atmospheric pressure (760 Torr) measured for $Hf_{0.5}Zr_{0.5}O_2$ resonators with L = 211.8 μm, W = 8.6 μm, and H = 10, 30, and 50 nm. Three regimes of Q behavior can be observed with (1) plateau where Q is not limited by air damping, (2) $Q \propto p^{-1}$ where Q is limited by FMF damping, and (3) $Q \propto p^{-1/2}$ where Q is limited by viscous damping.

To investigate and model the dissipations from TED, clamping loss, and surface loss, we first need to extract some basic properties of the resonators. Since the resonators have a huge length-to-thickness ratio ($L/H \gg 1$) with expected high residual tensile stress, the resonance frequency (f) for the fundamental out-of-plane flexural mode can be modeled using the string model (also confirmed by measured resonance frequency ratio in Table S2 in the Supporting Information)

$$f = \frac{1}{2L}\sqrt{\frac{\sigma}{\rho}} \tag{2}$$

where σ is the built-in stress and ρ = 7768 kg/m^3 is the mass density of the composite material.[15] Thus, by comparing the curves produced by eq 2 with the measured resonance frequencies in Figure 4a, we extract the built-in tensile stress of $Hf_{0.5}Zr_{0.5}O_2$ resonators with different thicknesses: $\sigma \approx 600$ MPa for H = 50 nm, $\sigma \approx 250$ MPa for H = 30 nm, and $\sigma \approx$ 0.2−2 MPa for H = 10 nm. The higher stress in thicker devices is introduced by the intercalated Al_2O_3 layers. We can further measure the temperature-dependent resonance frequency of $Hf_{0.5}Zr_{0.5}O_2$ resonators to extract its temperature coefficient of frequency (TCf), from which we can calculate the thermal expansion coefficient α of the device with different thicknesses using the equation (with the assumption of identical α in different directions, see detailed derivation in the Supporting Information)[25]

$$\alpha = \alpha_{Sub} - \frac{4Lf\sqrt{\rho\sigma}\,TCf}{E_Y} \tag{3}$$

where α_{Sub} = 2.6 ppm/°C is the thermal expansion coefficient of the silicon substrate and E_Y = 320 GPa is Young's modulus of the laminated structure.[15] Figure 4b shows the temperature-

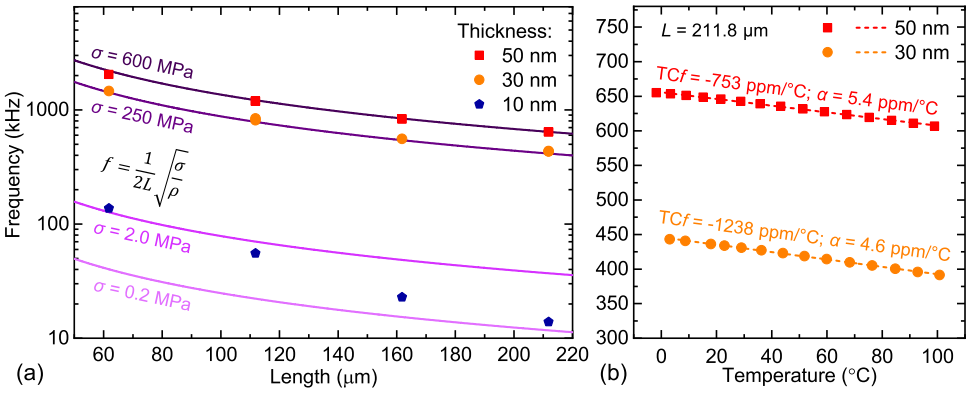

Figure 4. Evaluation of mechanical and thermal properties of $Hf_{0.5}Zr_{0.5}O_2$ resonators. (a) Scaling of f vs L at different σ levels. Scattered symbols represent the measured f from devices with different H; while curves show the theoretical frequencies based on the string model eq 2. (b) Extraction of α by measuring the TCf of the 50 and 30 nm thick devices. Symbols represent measured data and dashed lines show the linear fitting of the data.

https://doi.org/10.1021/acsami.2c08414
ACS Appl. Mater. Interfaces 2022, 14, 36807−36814

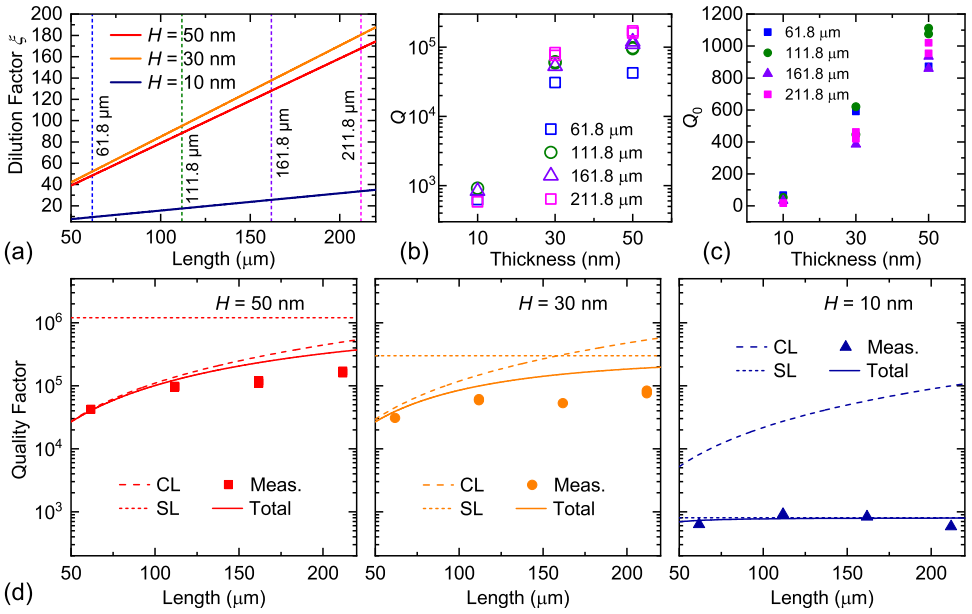

Figure 5. High Q of the superlattice $Hf_{0.5}Zr_{0.5}O_2$ resonators and its limiting dissipation mechanisms. (a) Dilution factor variation upon different lengths for $Hf_{0.5}Zr_{0.5}O_2$ resonators with different thicknesses. (b) Measured Q vs H of $Hf_{0.5}Zr_{0.5}O_2$ resonators. (c) Q_0 vs H of $Hf_{0.5}Zr_{0.5}O_2$ resonators. (d) Comparison of measured Qs and evaluated Qs limited by clamping loss (CL) and surface loss (SL) and total loss for H = 50, 30, and 10 nm devices, respectively.

dependent frequency for temperature T = 0 to 100 °C with linear fitting to extract TCf and α of the devices. H = 30 nm has lower α (=4.6 ppm/°C) than the α (=5.4 ppm/°C) of H = 50 nm device. The difference in α can be explained by the higher proportion of Al_2O_3 in H = 50 nm devices (~8.0%) than that in H = 30 nm devices (~6.8%) since Al_2O_3 has a higher α of 8.4 ppm/°C. The thermal expansion coefficient of the $Hf_{0.5}Zr_{0.5}O_2$-Al_2O_3 structure can be utilized for the analysis of TED of the $Hf_{0.5}Zr_{0.5}O_2$ resonators.

Q is the parameter that describes the energy dissipation process in a resonator. For a mechanical resonator, Q is defined as

$$Q = 2\pi\frac{U}{\Delta U} \tag{4}$$

where U is the total mechanical energy stored in the resonant mode and ΔU is the energy dissipated per cycle. The mechanical energy consists of three parts: the first two due to bending at antinodes $U_{\text{Bend-Str}}$ (string-like) and clamping point $U_{\text{Bend-Cant}}$ (cantilever-like), and the other one due to stress-induced elongation U_{Elong}, $U = U_{\text{Bend-Cant}} + U_{\text{Bend-Str}} + U_{\text{Elong}}$. These three components can be written as[26−28]

$$\begin{cases} U_{\text{Bend-Str}} = \dfrac{1}{2}E_Y I\displaystyle\int_0^L [u''(x)]^2 dx \\ U_{\text{Bend-Cant}} = \dfrac{1}{2}E_Y I\displaystyle\int_0^L [v''(x)]^2 dx \\ U_{\text{Elong}} = \dfrac{1}{2}\sigma A\displaystyle\int_0^L [u'(x)]^2 dx \end{cases} \tag{5}$$

where $u(x) = \delta z \sin(\pi x/L)$ is the mode shape of a string resonator, δz is the displacement of the resonator, $I = WH^3/12$ is the moment of inertia, $v(x) = \delta z\, \pi[(\sigma A)/(6E_Y IL)]x^2(3L_C - x)$ is the cantilever-like mode shape at the clamping points, $L_C = [(2E_Y I)/(\sigma A)]^{1/2}$ is the cantilever length,[26] and $A = WH$ is the cross-sectional area of the device. By completing the integration in eq 5, we have

$$\begin{cases} U_{\text{Bend-Str}} = \delta z^2\dfrac{\pi^4 E_Y I}{4L^3} \\ U_{\text{Bend-Cant}} = \delta z^2\dfrac{\pi^2\sqrt{2\sigma A E_Y I}}{3L^2} \\ U_{\text{Elong}} = \delta z^2\dfrac{\pi^2\sigma A}{4L} \end{cases} \tag{6}$$

According to eq 4, U_{Elong} is diluting the energy dissipation in the $Hf_{0.5}Zr_{0.5}O_2$ resonators. When only bending terms exist, the dissipation is undiluted. We define the quality factor without dissipation dilution as Q_0. Then, we have dilution factor $\xi = Q/Q_0 = U/(U_{\text{Bend-Cant}} + U_{\text{Bend-Str}})$. It is easy to estimate that $U_{\text{Elong}} \gg (U_{\text{Bend-Cant}} + U_{\text{Bend-Str}})$ for all $Hf_{0.5}Zr_{0.5}O_2$ resonators in this work, so we have $U \approx U_{\text{Elong}}$ and $\xi \approx U_{\text{Elong}}/(U_{\text{Bend-Cant}} + U_{\text{Bend-Str}})$. Considering the results from eq 6, we have

$$Q = \xi Q_0 = \left(\frac{8\sqrt{2}}{3}\lambda + \pi^2\lambda^2\right)^{-1} Q_0 \tag{7}$$

where $\lambda = (H/L)[E_Y/(12\sigma)]^{1/2}$. Using eq 7, we plot the dilution factor for the devices measured in this work in Figure 5a. ξ ranges from 9 to 34 for 10 nm thick devices and from ~50 to ~180 for 30 and 50 nm thick devices (see Table S3 in the Supporting Information for details), inducing significant Q enhancement.

Scattered symbols in Figure 5b show the measured Qs all at p < 5 mTorr for devices at different thicknesses and lengths, respectively. The thicker devices (H = 30 and 50 nm), where Al_2O_3 is introduced for higher built-in stress, have much higher Qs than the thinner counterparts (H = 10 nm), indicating that the higher stress promotes higher Q. By removing the dissipation dilution effects, we plot the Q_0 of all devices in

https://doi.org/10.1021/acsami.2c08414
ACS Appl. Mater. Interfaces 2022, 14, 36807−36814

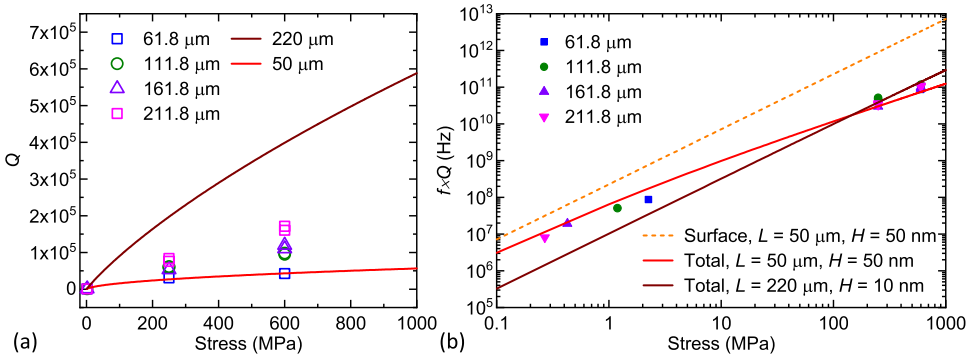

Figure 6. (a) Projection of Q for $Hf_{0.5}Zr_{0.5}O_2$ superlattice resonators with varying built-in stress. (b) Scaling of $f \times Q$ at varying stress. Scattered symbols are measured values. Solid curves represent calculated values considering both surface and clamping losses, while the orange dashed curve shows the calculated $f \times Q$ when only the surface loss is considered.

Figure 5c. The Q_0 still follows the trend of higher Q in thicker devices; however, there is no clear dependence on the length of the resonator.

Based on the trends, we can evaluate the limiting damping mechanisms in these resonators. First, we calculate the TED-limited Q for $Hf_{0.5}Zr_{0.5}O_2$ nanomechanical resonators. The exact expression for TED in vibrating strings (narrow membrane) is[29]

$$(Q)^{-1}_{\mathrm{TED}} = \frac{E_Y \alpha^2 T}{\rho C_p}\left(\frac{6}{\xi^2} - \frac{6}{\xi^2}\frac{\sin h\,\xi + \sin\xi}{\cos h\,\xi + \cos\xi}\right), \quad \xi = H\sqrt{\frac{\pi f \rho C_p}{\kappa}} \tag{8}$$

where T = 300 K is the temperature, C_p = 279 J/(K kg) is the mass heat capacity,[30] and κ = 0.72 W/(m K) is the thermal conductivity.[31] Since the thermal properties of $Hf_{0.5}Zr_{0.5}O_2$ are not readily available, except for the thermal expansion coefficient measured in Figure 4b, we use the values from thin-film tetragonal HfO_2 to estimate the TED-limited Q of the $Hf_{0.5}Zr_{0.5}O_2$ resonators. The estimated TED-limited Qs are plotted with dashed-dotted lines in Figure S5 in the Supporting Information, which are significantly higher than the measured values. By further considering the stress effect, these numbers will be even higher, thus TED-limited Q can be neglected.[26]

Clamping loss is the result of elastic waves of the resonator radiating into the anchor of the device. The empirical relation of the out-of-plane flexural modes for doubly clamped, thin-film resonators is $Q_{\mathrm{Clamping}} \propto L/W$.[32,33] By adding the stress-induced dissipation dilution as derived earlier from eq 7, we have $Q_{\mathrm{Clamping}} \propto \xi L/W$. If we assume $Q_{\mathrm{Clamping}} = 120\xi L/W$, we can plot the clamping loss limited Q with dashed lines in Figure 5d.

Surface loss arises from the phonon scattering at the surface of the device. The exact theoretical analysis or model for surface loss mechanisms have yet to be comprehensively established. Intuitively, one expects the dissipation to be proportional to the surface area of the device. We can write the surface loss per cycle

$$\Delta U_{\mathrm{Surface}} = \beta \cdot 2(LW + LH) \approx 2\beta LW \tag{9}$$

where $H \ll W$ and β is an assumed constant damping coefficient. Thus, using U_{Elong} ($\approx U$) in eq 6 and combining eqs 4 and 9, we can get surface-loss-limited Q

$$\left(\frac{1}{Q}\right)_{\mathrm{Surface}} = \frac{2\beta LW}{2\pi\delta z \frac{\pi^2 \sigma WH}{4L}} = \frac{4\beta L^2}{\pi^3 \delta z^2 \sigma H} \tag{10}$$

We can assume that $\delta z/L$ is constant given their relation. Then, we have $Q_{\mathrm{Surface}} \propto \sigma H$. We define $Q_{\mathrm{Surface}} = B\sigma H$ and assume B = 40,000 m/N. By plotting calculated Q_{Surface} with short-dashed lines in Figure 5d, we notice a different trend from Qs limited by the clamping loss which increases with the increasing length of the device, compared to surface-limited Q, which is irrelevant to the length of the device. Thus, if the total Q is not increasing with length, Q_{Surface} may be the main limiting factor of the total Q, which is the case for measured Q of H = 10 nm devices.

By assuming that $(1/Q)_{\mathrm{TED}}$, $(1/Q)_{\mathrm{Air}}$, and $(1/Q)_{\mathrm{Other}}$ are negligible, we evaluate the total Q with solid lines in Figure 5d, which agrees well with measured Qs. As suggested by the plots, for the devices with H = 50 nm, Q_{Total} is mainly limited by the clamping loss, for devices with H = 30 nm, Q_{Total} is limited by both clamping loss and surface loss, while for H = 10 nm devices, Q_{Total} is limited by surface loss. Thus, when stress is introduced by Al_2O_3 layers, clamping loss tends to be the dominant dissipation pathway, suggesting that by mitigating the clamping loss with engineering methods, the Q of the $Hf_{0.5}Zr_{0.5}O_2$ resonator can be much improved.

Given that the clamping loss and the surface loss are the limiting factors of Q, which both depend on σ in the device, it is worth analyzing the relation between Q and σ. Figure 6 shows the measured and calculated Q and $f \times Q$ at varying σ, where they both increase monotonically with increasing σ. Since the stress in the device is expected to originate from Al_2O_3 layers, the stress in the device can be enhanced through the alteration of the number and thickness of Al_2O_3 and modification of the thermal parameters during growth and RTA of the superlattice to increase the Q of $Hf_{0.5}Zr_{0.5}O_2$ resonators. In addition, since the major dissipation source for laminated devices (the thinnest H = 10 nm device has no Al_2O_3 layer) is clamping loss, methods to reduce the energy radiated to the substrate can significantly enhance Q and $f \times Q$ can reach 10^{12} Hz at σ > 500 MPa (when the surface loss is the limiting factor), as shown by the orange dashed line in Figure 6b. One method to reduce the energy radiated to the substrate is to add phononic structures at clamping locations with phononic forbidden bands at the resonance frequency (soft-clamping approach), leading to $U_{\mathrm{Bend\text{-}Cant}}$ term to diminish.[34,35] Such a method can be applied to $Hf_{0.5}Zr_{0.5}O_2$ resonators for a

https://doi.org/10.1021/acsami.2c08414
ACS Appl. Mater. Interfaces 2022, 14, 36807−36814

pure intrinsic dissipation source (TED or surface loss) with dominant high Qs.

CONCLUSIONS

We have demonstrated that the incorporation of Al_2O_3 interlayers in $Hf_{0.5}Zr_{0.5}O_2$ nanoelectromechanical resonators not only maintains the ferroelectricity of $Hf_{0.5}Zr_{0.5}O_2$ but also boosts the Q of the resonator, with the $f \times Q$ of the measured devices reaching 10^{11} Hz. Through analyses, clamping loss is determined to be the limiting dissipation pathway for superlattice $Hf_{0.5}Zr_{0.5}O_2$ resonators. Additional steps can be taken to further enhance the $f \times Q$ of $Hf_{0.5}Zr_{0.5}O_2$ NEMS resonators by 1 or more orders of magnitude, approaching the material-limited $f \times Q$. The extrapolated potential Qs of 100s at >10 GHz resonances are particularly promising for RF NEMS applications, high sensitivity resonant sensing, and possible room-temperature quantum optomechanics ($f \times Q \geq k_B T/\hbar = 6 \times 10^{12}$ Hz).

ASSOCIATED CONTENT

Supporting Information

The Supporting Information is available free of charge at https://pubs.acs.org/doi/10.1021/acsami.2c08414.

Electrical characterization of pristine $Hf_{0.5}Zr_{0.5}O_2$, GIXRD characterization of nanolaminate $Hf_{0.5}Zr_{0.5}O_2$, thermal expansion coefficient extraction from frequency shift, summary of device performance, and dissipation dilution factors (PDF)

AUTHOR INFORMATION

Corresponding Author

Roozbeh Tabrizian − *Department of Electrical and Computer Engineering, Herbert Wertheim College of Engineering, University of Florida, Gainesville, Florida 32611, United States;* orcid.org/0000-0003-1245-8564; Email: rtabrizian@ece.ufl.edu

Authors

Xu-Qian Zheng − *Department of Electrical and Computer Engineering, Herbert Wertheim College of Engineering, University of Florida, Gainesville, Florida 32611, United States;* orcid.org/0000-0003-4705-771X

Troy Tharpe − *Department of Electrical and Computer Engineering, Herbert Wertheim College of Engineering, University of Florida, Gainesville, Florida 32611, United States*

S M Enamul Hoque Yousuf − *Department of Electrical and Computer Engineering, Herbert Wertheim College of Engineering, University of Florida, Gainesville, Florida 32611, United States;* orcid.org/0000-0003-4307-3544

Nicholas G. Rudawski − *Research Service Centers, Herbert Wertheim College of Engineering, University of Florida, Gainesville, Florida 32611, United States*

Philip X.-L. Feng − *Department of Electrical and Computer Engineering, Herbert Wertheim College of Engineering, University of Florida, Gainesville, Florida 32611, United States;* orcid.org/0000-0002-1083-2391

Complete contact information is available at: https://pubs.acs.org/10.1021/acsami.2c08414

Notes

The authors declare no competing financial interest.

ACKNOWLEDGMENTS

The authors would like to thank the University of Florida Nanoscale Research Facility cleanroom staff for fabrication support. X.-Q.Z., T.T., and R.T. acknowledge the financial support from the Defense Advanced Research Projects Agency (DARPA) through the Young Faculty Award (Grant D19AP00044) and the National Science Foundation (NSF) through the CAREER award (Grant ECCS-1752206). X.-Q.Z., E.H.Y., and P.F. acknowledge the financial support from the NSF through the CAREER award (Grant ECCS-2015708) and EPMD program (Grant ECCS-2015670).

REFERENCES

(1) Böscke, T. S.; Müller, J.; Bräuhaus, D.; Schröder, U.; Böttger, U. Ferroelectricity in Hafnium Oxide Thin Films. *Appl. Phys. Lett.* **2011**, *99*, No. 102903.

(2) Lomenzo, P. D.; Alcala, R.; Richter, C.; Li, S.; Mikolajick, T.; Schroeder, U. Pyroelectric Dependence of Atomic Layer-Deposited $Hf_{0.5}Zr_{0.5}O_2$ on Film Thickness and Annealing Temperature. *Appl. Phys. Lett.* **2021**, *119*, No. 112903.

(3) Cheema, S. S.; Shanker, N.; Wang, L.-C.; Hsu, C.-H.; Hsu, S.-L.; Liao, Y.-H.; San Jose, M.; Gomez, J.; Chakraborty, W.; Li, W.; Bae, J.-H.; Volkman, S. K.; Kwon, D.; Rho, Y.; Pinelli, G.; Rastogi, R.; Pipitone, D.; Stull, C.; Cook, M.; Tyrrell, B.; Stoica, V. A.; Zhang, Z.; Freeland, J. W.; Tassone, C. J.; Mehta, A.; Saheli, G.; Thompson, D.; Suh, D. I.; Koo, W.-T.; Nam, K.-J.; Jung, D. J.; Song, W.-B.; Lin, C.-H.; Nam, S.; Heo, J.; Parihar, N.; Grigoropoulos, C. P.; Shafer, P.; Fay, P.; Ramesh, R.; Mahapatra, S.; Ciston, J.; Datta, S.; Mohamed, M.; Hu, C.; Salahuddin, S. Ultrathin Ferroic HfO_2−ZrO_2 Superlattice Gate stack for Advanced Transistors. *Nature* **2022**, *604*, 64−71.

(4) Mulaosmanovic, H.; Ocker, J.; Müller, S.; Schroeder, U.; Müller, J.; Polakowski, P.; Flachowsky, S.; van Bentum, R.; Mikolajick, T.; Slesazeck, S. Switching Kinetics in Nanoscale Hafnium Oxide Based Ferroelectric Field-Effect Transistors. *ACS Appl. Mater. Interfaces* **2017**, *9*, 3792−3798.

(5) Mikolajick, T.; Slesazeck, S.; Park, M. H.; Schroeder, U. Ferroelectric Hafnium Oxide for Ferroelectric Random-Access Memories and Ferroelectric Field-Effect Transistors. *MRS Bull.* **2018**, *43*, 340−346.

(6) Park, M. H.; Lee, Y. H.; Mikolajick, T.; Schroeder, U.; Hwang, C. S. Review and Perspective on Ferroelectric HfO_2-Based Thin Films for Memory Applications. *MRS Commun.* **2018**, *8*, 795−808.

(7) Max, B.; Hoffmann, M.; Mulaosmanovic, H.; Slesazeck, S.; Mikolajick, T. Hafnia-Based Double-Layer Ferroelectric Tunnel Junctions as Artificial Synapses for Neuromorphic Computing. *ACS Appl. Electron. Mater.* **2020**, *2*, 4023−4033.

(8) Park, M. H.; Kim, H. J.; Kim, Y. J.; Moon, T.; Kim, K. D.; Hwang, C. S. Thin $Hf_xZr_{1-x}O_2$ Films: A New Lead-Free System for Electrostatic Supercapacitors with Large Energy Storage Density and Robust Thermal Stability. *Adv. Energy Mater.* **2014**, *4*, No. 1400610.

(9) Hoffmann, M.; Schroeder, U.; Kunneth, C.; Kersch, A.; Starschich, S.; Bottger, U.; Mikolajick, T. Ferroelectric Phase Transitions in Nanoscale HfO_2 Films Enable Giant Pyroelectric Energy Conversion and Highly Efficient Supercapacitors. *Nano Energy* **2015**, *18*, 154−164.

(10) Starschich, S.; Schenk, T.; Schroeder, U.; Boettger, U. Ferroelectric and Piezoelectric Properties of $Hf_{1-x}Zr_xO_2$ and Pure ZrO_2 Films. *Appl. Phys. Lett.* **2017**, *110*, No. 182905.

(11) Ghatge, M.; Walters, G.; Nishida, T.; Tabrizian, R. An Ultrathin Integrated Nanoelectromechanical Transducer Based on Hafnium Zirconium Oxide. *Nat. Electron.* **2019**, *2*, 506−512.

(12) Ghatge, M.; Walters, G.; Nishida, T.; Tabrizian, R. A 30-nm Thick Integrated Hafnium Zirconium Oxide Nano-Electro-Mechanical Membrane Resonator. *Appl. Phys. Lett.* **2020**, *116*, No. 043501.

(13) Müller, J.; Böscke, T. S.; Schröder, U.; Mueller, S.; Bräuhaus, D.; Böttger, U.; Frey, L.; Mikolajick, T. Ferroelectricity in Simple Binary ZrO_2 and HfO_2. *Nano Lett.* **2012**, *12*, 4318−4323.

(14) Park, M. H. H.; Kim, H. J.; Kim, Y. J.; Lee, W.; Moon, T.; Hwang, C. S. Evolution of Phases and Ferroelectric Properties of Thin $Hf_{0.5}Zr_{0.5}O_2$ Films According to the Thickness and Annealing Temperature. *Appl. Phys. Lett.* **2013**, *102*, No. 242905.
(15) Tharpe, T.; Zheng, X.-Q.; Feng, P. X.-L.; Tabrizian, R. Resolving Mechanical Properties and Morphology Evolution of Free-Standing Ferroelectric $Hf_{0.5}Zr_{0.5}O_2$. *Adv. Eng. Mater.* **2021**, *23*, No. 2101221.
(16) Roukes, M. L. In *Nanoelectromechanical Systems*, Tech. Digest 2000 Solid-State Sens. Actuator Workshop; Hilton Head, 2000.
(17) Lee, J.; Wang, Z.; He, K.; Yang, R.; Shan, J.; Feng, P. X.-L. Electrically Tunable Single- and Few-Layer MoS_2 Nanoelectromechanical Systems with Broad Dynamic Range. *Sci. Adv.* **2018**, *4*, 27−35.
(18) Fan, X.; Forsberg, F.; Smith, A. D.; Schröder, S.; Wagner, S.; Rödjegård, H.; Fischer, A. C.; Östling, M.; Lemme, M. C.; Niklaus, F. Graphene Ribbons with Suspended Masses as Transducers in Ultra-Small Nanoelectromechanical Accelerometers. *Nat. Electron.* **2019**, *2*, 394−404.
(19) Fields, S. S.; Olson, D. H.; Jaszewski, S. T.; Fancher, C. M.; Smith, S. W.; Dickie, D. A.; Esteves, G.; Henry, M. D.; Davids, P. S.; Hopkins, P. E.; Ihlefeld, J. F. Compositional and Phase Dependence of Elastic Modulus of Crystalline and Amorphous $Hf_{1-x}Zr_xO_2$ Thin Films. *Appl. Phys. Lett.* **2021**, *118*, No. 102901.
(20) Riedel, S.; Polakowski, P.; Müller, J. A Thermally Robust and Thickness Independent Ferroelectric Phase in Laminated Hafnium Zirconium Oxide. *AIP Adv.* **2016**, *6*, No. 095123.
(21) Hakim, F.; Tharpe, T.; Tabrizian, R. Ferroelectric-on-Si Super-High-Frequency Fin Bulk Acoustic Resonators with $Hf_{0.5}Zr_{0.5}O_2$ Nanolaminated Transducers. *IEEE Microw. Wirel. Compon. Lett.* **2021**, *31*, 701−704.
(22) Kim, H. J.; Park, M. H.; Kim, Y. J.; Lee, Y. H.; Jeon, W.; Gwon, T.; Moon, T.; Kim, K. D.; Hwang, C. S. Grain Size Engineering for Ferroelectric $Hf_{0.5}Zr_{0.5}O_2$ Films by an Insertion of Al_2O_3 Interlayer. *Appl. Phys. Lett.* **2014**, *105*, No. 192903.
(23) Ghaffari, S.; Chandorkar, S. A.; Wang, S.; Ng, E. J.; Ahn, C. H.; Hong, V.; Yang, Y.; Kenny, T. W. Quantum Limit of Quality Factor in Silicon Micro and Nano Mechanical Resonators. *Sci. Rep.* **2013**, *3*, No. 3244.
(24) Lee, J.; Wang, Z.; He, K.; Shan, J.; Feng, P. X.-L. Air Damping of Atomically Thin MoS_2 Nanomechanical Resonators. *Appl. Phys. Lett.* **2014**, *105*, No. 023104.
(25) Larsen, T.; Schmid, S.; Grönberg, L.; Niskanen, A. O.; Hassel, J.; Dohn, S.; Boisen, A. Ultrasensitive String-Based Temperature Sensors. *Appl. Phys. Lett.* **2011**, *98*, No. 121901.
(26) Schmid, S.; Jensen, K. D.; Nielsen, K. H.; Boisen, A. Damping Mechanisms in High-Q Micro and Nanomechanical String Resonators. *Phys. Rev. B* **2011**, *84*, No. 165307.
(27) Unterreithmeier, Q. P.; Faust, T.; Kotthaus, J. P. Damping of Nanomechanical Resonators. *Phys. Rev. Lett.* **2010**, *105*, No. 027205.
(28) Villanueva, L. G.; Schmid, S. Evidence of Surface Loss as Ubiquitous Limiting Damping Mechanism in SiN Micro- and Nanomechanical Resonators. *Phys. Rev. Lett.* **2014**, *113*, No. 227201.
(29) Lifshitz, R.; Roukes, M. L. Thermoelastic Damping in Micro- and Nanomechanical Systems. *Phys. Rev. B* **2000**, *61*, No. 5600.
(30) Low, J. J.; Paulson, N. H.; D'Mello, M.; Stan, M. Thermodynamics of Monoclinic and Tetragonal Hafnium Dioxide (HfO_2) at Ambient Pressure. *Calphad* **2021**, *72*, No. 102210.
(31) Panzer, M. A.; Shandalov, M.; Rowlette, J. A.; Oshima, Y.; Chen, Y. W.; McIntyre, P. C.; Goodson, K. E. Thermal Properties of Ultrathin Hafnium Oxide Gate Dielectric Films. *IEEE Electron Device Lett.* **2009**, *30*, 1269−1271.
(32) Cross, M. C.; Lifshitz, R. Elastic Wave Transmission at an Abrupt Junction in a Thin Plate with Application to Heat Transport and Vibrations in Mesoscopic Systems. *Phys. Rev. B* **2001**, *64*, No. 085324.
(33) Judge, J. A.; Photiadis, D. M.; Vignola, J. F.; Houston, B. H.; Jarzynski, J. Attachment Loss of Micromechanical and Nanomechanical Resonators in the Limits of Thick and Thin Support Structures. *J. Appl. Phys.* **2007**, *101*, No. 013521.
(34) Tsaturyan, Y.; Barg, A.; Polzik, E. S.; Schliesser, A. Ultracoherent Nanomechanical Resonators via Soft Clamping and Dissipation Dilution. *Nat. Nanotechnol.* **2017**, *12*, 776−784.
(35) Ghadimi, A. H.; Fedorov, S. A.; Engelsen, N. J.; Bereyhi, M. J.; Schilling, R.; Wilson, D. J.; Kippenberg, T. J. Elastic Strain Engineering for Ultralow Mechanical Dissipation. *Science* **2018**, *360*, 764−768.

https://doi.org/10.1021/acsami.2c08414
ACS Appl. Mater. Interfaces 2022, 14, 36807−36814